catalysts

MDPI

Article

Innovative Production of 3D-Printed Ceramic Monolithic Catalysts for Oxidation of VOCs by Using Fused Filament Fabrication

Filip Car *, Nikolina Zekić, Domagoj Vrsaljko * and Vesna Tomašić

Faculty of Chemical Engineering and Technology, University of Zagreb, Marulićev trg 19, 10000 Zagreb, Croatia; nzekic@fkit.unizg.hr (N.Z.); vtomas@fkit.unizg.hr (V.T.)
* Correspondence: fcar@fkit.unizg.hr (F.C.); dvrsal@fkit.unizg.hr (D.V.)

Abstract: In this work, ceramic monolithic catalyst carriers based on zirconium dioxide (ZrO_2) were produced using fused filament fabrication (FFF). The active catalyst components were deposited on the resulting carriers using the wet impregnation method. The activity of the prepared monolithic catalysts was evaluated by catalytic oxidation of a mixture of aromatic volatile organic compounds: benzene, toluene, ethylbenzene, and *o*-xylene (BTEX). The efficiency of the prepared monolithic catalysts was investigated as a function of the geometry of the monolithic carrier (ZDP, Z, and M) and the chemical composition of the catalytically active component ($MnFeO_x$, $MnCuO_x$, and $MnNiO_x$) during the catalytic oxidation of BTEX compounds. The mechanical stability of the catalyst layer and the dimensional stability of the 3D-printed monolithic catalyst carriers were investigated prior to the kinetic measurements. In addition, thorough characterization of the commercial ZrO_2-based filament was carried out. The results of the efficiency of the prepared monolithic catalysts for the catalytic oxidation of BTEX showed that the 3D-printed model M, which contained $MnFeO_x$ as the catalytically active component, was the most successful catalyst for the oxidation of BTEX compounds. The mentioned catalyst enables the catalytic oxidation of all components of the BTEX mixture (>99% efficiency) at a temperature of 177 °C.

Keywords: additive manufacturing (AM); fused filament fabrication (FFF); monolithic catalyst; catalytic oxidation; benzene; toluene; ethylbenzene; *o*-xylene

Academic Editors: Federico Galli and Wen Ma

Received: 20 December 2024
Revised: 23 January 2025
Accepted: 25 January 2025
Published: 27 January 2025

Citation: Car, F.; Zekić, N.; Vrsaljko, D.; Tomašić, V. Innovative Production of 3D-Printed Ceramic Monolithic Catalysts for Oxidation of VOCs by Using Fused Filament Fabrication. *Catalysts* **2025**, *15*, 125. https://doi.org/10.3390/catal15020125

1. Introduction

Additive manufacturing (AM), also known as 3D printing, is a widely recognized technology that enables fast and easy production of complex structures at low cost [1,2]. One of the advantages of additive manufacturing is the ability to work with a variety of materials, including metals [3,4], ceramics [5], polymers [6], and composites [7]. Using this method, 3D objects are produced by adding material layer by layer, which makes it easier to fabricate complex structures compared to conventional methods, such as drilling, turning, molding, etc. For these reasons, additive manufacturing is also used in the field of chemical engineering. This technology enables the production of monolithic structures with numerous channels in the millimeter range, resulting in low pressure drop and improved mass transfer during mixture flow through such a structure [8]. Großmann et al. [9] investigated the influence of different 3D-printed shapes on catalyst carriers and their wet impregnation with a platinum precursor. According to the results obtained, the monolithic

structures showed significantly higher activities for the dehydrogenation of perhydrodibenzyl toluene compared to cylinders with the same catalyst loading and similar reactor volume. This led to a reduction in the very expensive platinum loading, while the reactor volume remained constant, resulting in lower operating costs. In addition to catalysis, additive manufacturing is also used in aerospace industry [10], automotive industry [11], pharmaceutical industry [12], and in the medical field (dentistry and orthopedics) [13]. One of the most popular additive manufacturing techniques/methods is known as fused filament fabrication (FFF). In this process, the material is pushed through a heated nozzle and selectively deposited layer by layer on the building platform to create a 3D object [14].

This modern production technique proved to be simpler, faster, and even more economically acceptable than traditional techniques for producing complex structures. The main advantage of AM is the great flexibility in creating well-defined shapes with or without various internal structures, as well as the ability to quickly create complex prototypes. Reducing the time and cost of manufacturing monolithic structures with complex geometry (which is often the result of prior theoretical simulations) is extremely important, as it enables the development of innovative technologies and their rapid introduction into pre-commercial and commercial applications. Despite the great attractiveness of this technique, the information available in the literature on the application of FFF technology in heterogeneous catalysis is limited.

In this work, FFF was used as an innovative method for the preparation of ceramic monolithic catalyst carriers with complex geometry. Generally, monolithic structures are continuous, uniform structures that consist of many narrow and parallel channels or passages. Monolithic catalysts have several advantages over conventional catalysts, including better mass transfer, lower pressure drop, higher thermal stability, and good mechanical properties. These structures can be extruded into a wide range of shapes and sizes, including circular, square, triangular, and hexagonal shapes, using various materials. As mentioned above, monoliths are most commonly produced as ceramic or metallic structures [15]. Some solid catalysts consist only of the active component and the carrier, while most solid catalysts consist of three components: the active component, the catalyst support layer, and the carrier. The catalyst support layer can be applied to the monolithic structure to increase its surface area and to provide better adhesion and dispersion of the catalytically active components. This process is commonly known as washcoating. If the catalyst has sufficient mechanical and thermal strength, the catalyst material and some binder components can be extruded together into a monolithic shape. Some of the most common methods for depositing catalytically active layers on a monolithic carrier are wet impregnation, ion exchange, precipitation, coprecipitation, and sol–gel method [16–19].

Monolithic catalysts have a very important role in the treatment of volatile organic compounds (VOCs) emitted by industry because of their advantages such as good mass transfer performance, low pressure drop, good thermal stability, and high mechanical strength. VOCs are defined as organic compounds with a boiling point lower than 250 °C at a standard atmospheric pressure of 101.325 kPa. Due to their high volatility, mobility, and strong resistance to degradation, VOCs can travel great distances in the environment after being released. VOCs have an adverse effect on human health due to their influence on air quality caused by gas phase photochemical reactions that result in the formation of secondary pollutants like ground-level ozone and secondary aerosols. Catalytic combustion is the process of VOCs oxidation at low temperatures to produce CO/CO_2 and H_2O with the help of oxidation catalysts [20–24]. The essential component of catalytic oxidation is a catalyst, which directly determines how effectively VOCs are oxidized. Generally, they can be divided into noble metal catalysts, such as Pt, Pd, Rh, and Au, and non-noble metal catalysts, such as Fe, Co, and Mn. Noble-metal-based catalysts are widely used because

of their oxidation efficiency, a long service life, low dosage, and anti-corrosion properties. However, they are very expensive and susceptible to sintering and poisoning. On the other side, non-noble metal catalysts have advantage of high catalytic activity, availability, low cost, stability, and resistance to poisoning [25–27]. According to Xu et al. [28], one of the most promising heterogeneous catalysts is manganese oxide because of its properties such as low cost, environmental friendliness, and high catalytic oxidation performance. Oxides based on manganese have been frequently utilized as catalysts to remove gaseous pollutants. Generally, in oxidation reactions for VOC control, transition metal oxides have demonstrated highly effective catalytic performances. Kim et al. [29] studied the efficiency of manganese oxides (Mn_3O_4, Mn_2O_3, and MnO_2) in the catalytic combustion of VOCs (benzene and toluene). Research has shown that catalysts with high oxygen mobility and a high surface area are more catalytically active. Therefore, the catalytic activity of the studied catalysts was in the order $Mn_3O_4 > Mn_2O_3 > MnO_2$.

The aim of this work is to produce ceramic monolithic catalyst carriers based on zirconium dioxide (ZrO_2) using the fused filament fabrication technique. The active catalyst components were deposited on the resulting carriers using a wet impregnation technique. The dimensional stability of the 3D-printed monolithic carriers and the mechanical stability of the catalyst layer were investigated, as well as the characterization of the ZrO_2-based filament. Finally, the efficiency of the prepared monolithic catalysts for the catalytic oxidation of BTEX was determined with respect to the chemical composition of the catalytically active component ($MnFeO_x$, $MnCuO_x$, and $MnNiO_x$) and in relation to the geometry of the monolithic carriers (ZDP, Z, and M).

2. Results and Discussion

2.1. Preparation of Monolithic Catalyst Carriers

CAD models of catalyst carriers with ZDP and Z geometry were fully drawn using Autodesk Fusion 360, v.2.0.19941 (Figure 1), while M geometry was drawn as a cylinder without channels, which were subsequently added as 80% infill using Z-SUITE slicer, v.3.5 (Figure S1).

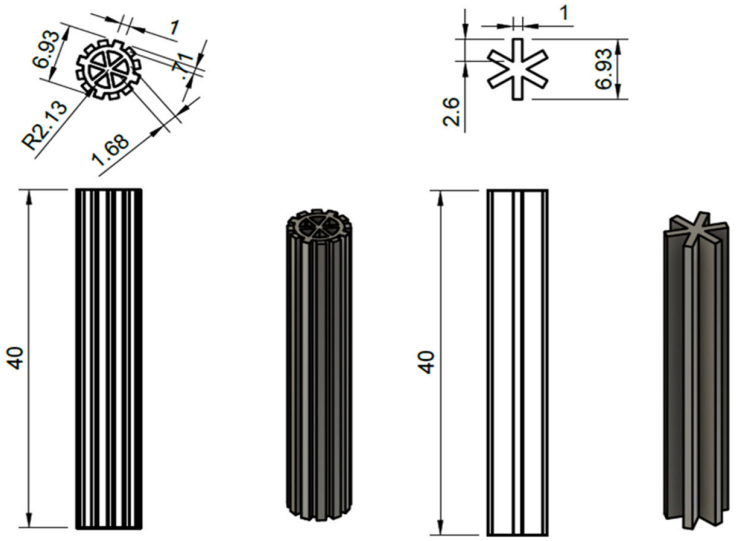

Figure 1. CAD models of 3D-printed catalyst carriers ZDP (left) and Z (right).

2.1.1. Determining the Optimal Printing Settings

Determination of optimal 3D printing settings began with the default settings listed in Table 1. A nozzle with a diameter of 0.5 mm was used for 3D printing, and an automatic

support structure was selected. The dimensions of the printed models were 7 mm × 10 mm, and the ZDP geometry was chosen.

Table 1. Default settings for 3D printing.

Extruder Flow Ratio, EFR	0% (default value)
Layer Thickness, LT	0.14 mm
Print Speed, PS	0% (default value)
Fan Speed, FS	20%
Density of the internal structure of the model (Infill)	Solid, 100%

The model 3D-printed with the specified settings is shown in Figure 1. During preparation for the 3D printing, it was immediately seen that the filament was very brittle, which led to difficulties in loading the material and, subsequently, in the 3D printing process itself. Due to the frequent cracking of the filament, constant monitoring was necessary. Figure S2 shows that the default 3D printing settings used are not satisfactory, since the channels inside the fabricated catalyst carrier are not visible, i.e., they were blocked with the softened filament.

To determine the optimal EFR, the models were printed with different EFR settings (−20%, −40%, and −50%), while keeping the other settings unchanged. The printed models are shown in Figure S3. It can be seen that the channels are most clearly defined on the model at an EFR of −40%. Therefore, the specified EFR is determined to be optimal. In the next step, the optimal PS was determined. The PS settings used to print the model were −20%, −40%, −50%, +20%, +40%, and +50%.

It was found that changes in PS in this case did not have a significant impact on the appearance of the printed models, so the default PS (0%) was chosen as optimal. Then, the optimal LT was determined. In addition to the default print settings, several different LT settings were tried: 0.09 mm, 0.19 mm, 0.29 mm, and 0.39 mm, out of which 0.19 mm was chosen as the optimal LT, due to the fact that the carrier channels were most clearly defined.

As can be seen in Figure S3, channels of the carrier are still not clearly defined due to the smearing of the material during 3D printing. It is assumed that this is due to the slow cooling of the material during 3D printing. This problem was approached in two ways: by simultaneously 3D printing the same two catalyst carrier models on opposite sides of the building platform and increasing the fan speed (FS) to 100%. By 3D printing two models at the same time, the 3D printer is forced to move the extruder from one side of the building platform to the other, which in combination with the highest FS gives enough time for the layers to cool down. This method enables production of several models with high precision and accuracy. In addition, the nozzle diameter was changed from 0.5 mm to 0.4 mm to further reduce channel filling with the softened filament. By increasing the FS and printing the two models in parallel, a carrier with ZDP geometry (Figure S4) was obtained on which the channels were clearly defined, and at the same time, no smearing of the material or tilting of the structure occurred. Finally, based on the results, the optimal printing settings were determined (Table 2), which were used for printing the monolithic catalyst carriers used in this research.

Table 2. Optimal 3D printing settings.

Extruder Flow Ratio, EFR	−40%
Layer Thickness, LT	0.19 mm
Print Speed, PS	default value
Fan speed, FS	100%

2.1.2. Preparation of Monolithic Catalyst Carriers with Optimal Settings

Certain optimal settings were first used to print monolithic catalyst carriers of the ZDP and Z geometries (Figure S5).

An experimental monolithic catalyst carrier of geometry M was also prepared (Figure 2), and it was obtained by changing the density of the internal structure of the model (infill). First, a CAD model of a solid cylinder with dimensions of 7 mm × 40 mm was created, and the density settings of the model's internal structure were set to 80% in the Z-SUITE program (slicer). The model was enlarged by 20% on the *z*-axis, while it was enlarged by 80% on the x- and y-axes, since the outer wall of the carrier needs to be mechanically removed after 3D printing. The upper part of the model, the so-called lid, and the support structure was also removed mechanically. The other 3D printing settings and procedure were the same as for the previously produced Z and ZDP carriers.

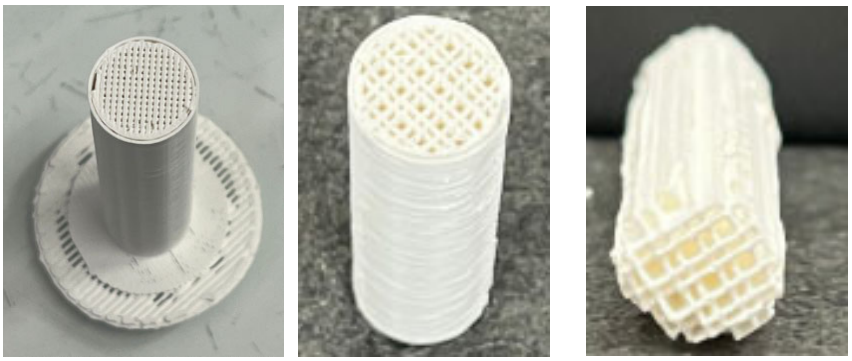

(**a**) (**b**) (**c**)

Figure 2. Monolithic catalyst carrier of geometry M (**a**) before mechanical processing, (**b**) after mechanical removal of the lid and support structure, and (**c**) after mechanical removal of the wall.

2.1.3. Application of Catalytically Active Components

Catalytically active components were applied to 3D-printed carriers using a wet impregnation technique. Monolithic catalysts turned black after calcination, indicating the formation of catalytically active mixed manganese oxides.

2.1.4. Testing the Dimensional and Mass Deviation of 3D-Printed Catalyst Carriers

The dimensional stability of the 3D-printed monolithic catalyst carriers was determined experimentally. Dimensional stability is a measure of model shrinkage during heat treatment. The deviation of the dimensions after heat treatment from the dimensions of the CAD model was determined by 3D printing and measuring five monolithic catalyst carriers of each geometry (ZDP, Z, and M) along the *x*-, *y*-, and *z*-axes using a digital caliper (Alpha Tools). The obtained results are shown in Table 3.

From the results obtained, it can be concluded that shrinkage of 20.08–21.65% in the *x*-axis direction, 20.09–21.86% in the *y*-axis direction, and 20.51–22.53% in the *z*-axis direction occurs during heat treatment (Table 3). The deviations obtained correspond well to the deviations specified by the manufacturer (21.2% ± 1% in the *x*-, *y*-, and *z*-axis). Based on the results obtained, a dimensional correction factor of 1.20 was determined, which must be taken into account when printing the carriers, since the lowest shrinkage was 20.08%. The mass loss of the 3D-printed catalyst carriers during heat treatment was also determined experimentally, and the results are shown in Table 4.

The mass losses obtained were between 14.28% and 15.13% (Table 4). The differences in the mass losses of the 3D-printed catalyst carriers were very small, which indicates an even distribution of the ceramic particles throughout the 3D-printed catalyst carriers.

Table 3. The results of the deviation tests of the dimensions of the 3D-printed carriers from the CAD model.

Geometry	Number of Carrier	Axis	CAD Model/mm	Heat Treated Model/mm	Shrinkage After Sintering/%
ZDP	1	x	8.40	6.62 ± 0.15	21.21
		y	8.40	6.59 ± 0.12	21.50
		z	48.00	37.19 ± 0.16	22.53
	2	x	8.40	6.58 ± 0.12	21.65
		y	8.40	6.60 ± 0.07	21.42
		z	48.00	37.42 ± 0.18	22.05
	3	x	8.40	6.63 ± 0.14	21.13
		y	8.40	6.61 ± 0.10	21.32
		z	48.00	38.16 ± 0.21	20.51
Z	1	x	8.40	6.71 ± 0.22	20.08
		y	8.40	6.56 ± 0.15	21.86
		z	48.00	37.27 ± 0.28	22.36
	2	x	8.40	6.59 ± 0.20	21.52
		y	8.40	6.62 ± 0.11	21.16
		z	48.00	37.33 ± 0.39	22.22
	3	x	8.40	6.61 ± 0.13	21.26
		y	8.40	6.71 ± 0.18	20.09
		z	48.00	37.39 ± 0.33	22.10
M	1	x	12.60	9.83 ± 0.21	22.00
		y	12.60	9.85 ± 0.16	21.79
		z	48.00	37.41 ± 0.38	22.06
	2	x	12.60	9.85 ± 0.13	21.81
		y	12.60	9.87 ± 0.27	21.69
		z	48.00	37.42 ± 0.30	22.04
	3	x	12.60	9.82 ± 0.11	22.09
		y	12.60	9.85 ± 0.17	21.84
		z	48.00	37.43 ± 0,34	22.02

Table 4. Test results of the mass loss of catalyst carriers during heat treatment.

Geometry	Number of Carrier	*m* (Green Body)/g	*m* (After Heat Treatment)/g	Mass Loss/%
ZDP	1	4.7612	4.0557	14.82
	2	4.6691	4.0025	14.28
	3	4.7253	4.0475	14.34
Z	1	3.5326	2.9981	15.13
	2	3.561	3.0269	15.00
	3	3.5187	2.9948	14.89
M	1	2.2735	1.9369	14.80
	2	2.2668	1.9288	14.91
	3	2.2799	1.9432	14.77

2.1.5. Adhesion Tests of Catalytic Layers

To perform the adhesion tests, five plates with CAD model dimensions of 20 mm × 10 mm × 2 mm were 3D-printed using the same principle. The 3D printing settings are shown in Table 5. The $MnFeO_x$ catalyst was applied to the 3D-printed plates using the wet impregnation, and the results of the adhesion tests are shown in Table 6.

Table 5. Three-dimensional printing settings for plates used in adhesion tests.

Extruder Flow Ratio, EFR	0% (default value)
Layer Thickness, LT	0.19 mm
Print Speed, PS	0% (default value)
Fan speed, FS	100%
Correction factor	1.20

Table 6. Mechanical stability of the $MnFeO_x$ layer on 3D-printed plates.

Plate Number	*m* (Before US Treatment)/g	*m* (After US Treatment)/g	Mass Loss/%
1	1.8831	1.8822	0.05
2	1.9705	1.9695	0.05
3	1.9436	1.9426	0.05
4	1.9181	1.9178	0.02
5	1.9445	1.9441	0.02

From the results obtained, it can be concluded that the loss of catalyst due to the effect of ultrasonic vibrations is insignificant (0.02–0.05%) (Table 6). As the adhesion test results point to an exceptional stability of the catalytic layer, the 3D-printed ceramic monolithic catalyst carriers (Z and ZDP geometry) with the applied catalytic layer can be safely used in the reactor system for the catalytic oxidation of BTEX compounds.

2.2. Characterizations

The composition of the used filament was determined by X-ray diffraction analysis, and the resulting diffractogram is shown in Figure S6. Characteristic peaks at 28°, 31°, 50°, and 60° can be observed on the spectrum, which indicates the monoclinic structure of ZrO_2 [30]. In addition to the peaks mentioned, additional peaks at 30° and 35° can be observed, which are characteristic of the tetragonal structure of ZrO_2 [31].

The size distribution of the ZrO_2-based filament ceramic particles was determined using the laser diffraction method (Figure S7). Ceramic particles were separated from the polymer matrix (filament) by quenching a filament sample in acetone for 24 h at room temperature. Ceramic particles were separated from the slurry by alternately using centrifuge (2 min at 8000 rpm) and rinsing with acetone for three consecutive times. Ceramic particles were then calcined at 500 °C for 3 h to remove any remaining polymer matrix.

Based on the results shown in Figure S7, the filament sample was found to contain particles of size 71–3000 µm. The value of the mean particle size (d_{50}) in the population is 540.10 µm. The predominant particle size in the population (d_{mode}) is 562.34 µm, while the Sauter diameter ($d_{3,2}$) of the particles is 886.25 µm.

The thermal properties of the ZrO_2-based filament were determined by TGA/DTA analysis, and the results are shown in Figure S8. The purple line shows the results of the TGA analysis, while the green line indicates the results of the DTA analysis. Based on the results obtained (Figure S8), the TGA curve can be divided into several areas. A peak shown on the DTA curve (green) below 100 °C indicates water loss. A mass decrease of about 14% can be observed between 200 and 500 °C, which can be attributed to degradation of the polymer phase. After 500 °C, no further mass change is observed, indicating that no further decomposition takes place. Two peaks can be seen on the DTA curve at a temperature of about 400 °C, indicating the loss of organic compounds, which can be associated with a mass loss of 14% on the TGA curve. Another exothermic peak can be observed at temperatures between 450–500 °C. This peak corresponds to a partial transition from the tetragonal to the monoclinic ZrO_2 structure [32,33].

The characteristic monolithic shape complicates the detailed characterization of monolithic catalysts due to the construction limitations of instrumental techniques, which generally allow the characterization of catalysts only in powder form. However, the results of extensive experimental and theoretical investigations of manganese-based metal oxides, $MnMO_x$ (M: Fe, Ni, and Cu) in powder form were reported previously [34]. Detailed characterization was performed for all three mixed metal oxides, including differential scanning calorimetry (DSC), nitrogen (N_2) adsorption–desorption analysis, scanning electron microscopy (SEM) with energy dispersive X-ray spectroscopy (EDS), temperature-programmed desorption of CO_2 (CO_2-TPD), temperature-programmed reduction of hydrogen (H_2-TPR), X-ray diffraction (XRD), and X-ray photoelectron spectroscopy (XPS). Insights into the phase composition, as well as the chemical composition and oxidation states, were obtained by X-ray diffraction (XRD) and X-ray photoelectron spectroscopy. Briefly, the results showed that MnO_2 and Mn_2O_3 are present in all samples except for $MnNiO_x$, where Mn_2O_3 was not observed. Besides manganese oxides, NiO and $MnNiO_3$ were detected in the $MnNiO_x$ sample and CuO and $CuMn_2O_4$ in the $MnCuO_x$ sample, while Fe_2O_3 or $FeMnO_3$ or both were present in the $MnFeO_x$ sample. The results of the XPS analysis were consistent with those of the XRD analysis, with the exception that the XRD analysis indicates the presence of additional oxides and double oxides such as $FeMnO_3$, $NiMnO_3$, and $CuMn_2O_4$. These differences can be explained by considering that XPS is a surface-sensitive method that provides information about the electronic states and chemical composition of the surface of a sample, while XRD is a bulk-sensitive analytical tool. Finally, based on the results of XRD and XPS analyses, which confirmed the presence of the characteristic α-MnO_2, α-Mn_2O_3, and Fe_2O_3 phases, it seems that the Mn^{4+}, Mn^{3+}, and Fe^{3+} sites are responsible for the high activity of the $MnFeO_x$ catalyst, although it is not easy to distinguish their contribution.

2.3. Catalytic Oxidation of BTEX Components

In the continuation of the research, the oxidation of BTEX compounds was carried out in a monolithic reactor to test the activity of prepared catalysts. First, the most efficient catalyst was determined with regards to the chemical composition of the catalytic layer ($MnFeO_x$, $MnNiO_x$, and $MnCuO_x$), and then the efficiency of the monolithic catalyst was determined with regards to the catalyst carrier geometry (ZDP and Z). The characteristic values of T_{10}, T_{50}, and T_{90}, i.e., the temperatures at which 10%, 50%, and 90% conversion of the BTEX compounds are achieved, were used as standard criteria for estimation of the catalyst efficiency. The masses of the catalytic layer applied to the monolithic carriers, as well as the dimensions of the carriers, are shown in Table 7. The results show that the measured values are approximately the same, with a slightly larger mass measured for $MnNiO_x$.

Table 7. Mass of the various catalytic layers applied on the catalyst carriers with ZDP geometry.

Geometry of the Monolithic Carrier	Number of the Catalyst Carrier	Dimensions/mm	Catalytic Layer	Mass of the Catalytic Layer/mg
ZDP	1	$6.58 \pm 0.12 \times 6.60 \pm 0.07 \times 37.42 \pm 0.18$	$MnFeO_x$	33.7
	2	$6.62 \pm 0.15 \times 6.59 \pm 0.12 \times 37.19 \pm 0.16$	$MnCuO_x$	33.3
	3	$6.63 \pm 0.14 \times 6.61 \pm 0.10 \times 37.77 \pm 0.17$	$MnNiO_x$	39.5

The catalytic activity of the prepared monolithic catalysts was tested in a reactor at atmospheric pressure, temperatures ranging from room temperature to 220 °C, and a constant flow rate of the reaction mixture of 92 cm^3/min. The corresponding WHSV (weight hourly space velocity) values for the monolithic geometries used in this study are

listed in Table S1. The initial concentration of benzene was 53.6 ppm, toluene 51.3 ppm, ethylbenzene 53.3 ppm, and *o*-xylene 50.7 ppm. The measurement results are shown in Figure 3, and the corresponding T_{10}, T_{50}, and T_{90} values are listed in Table 8.

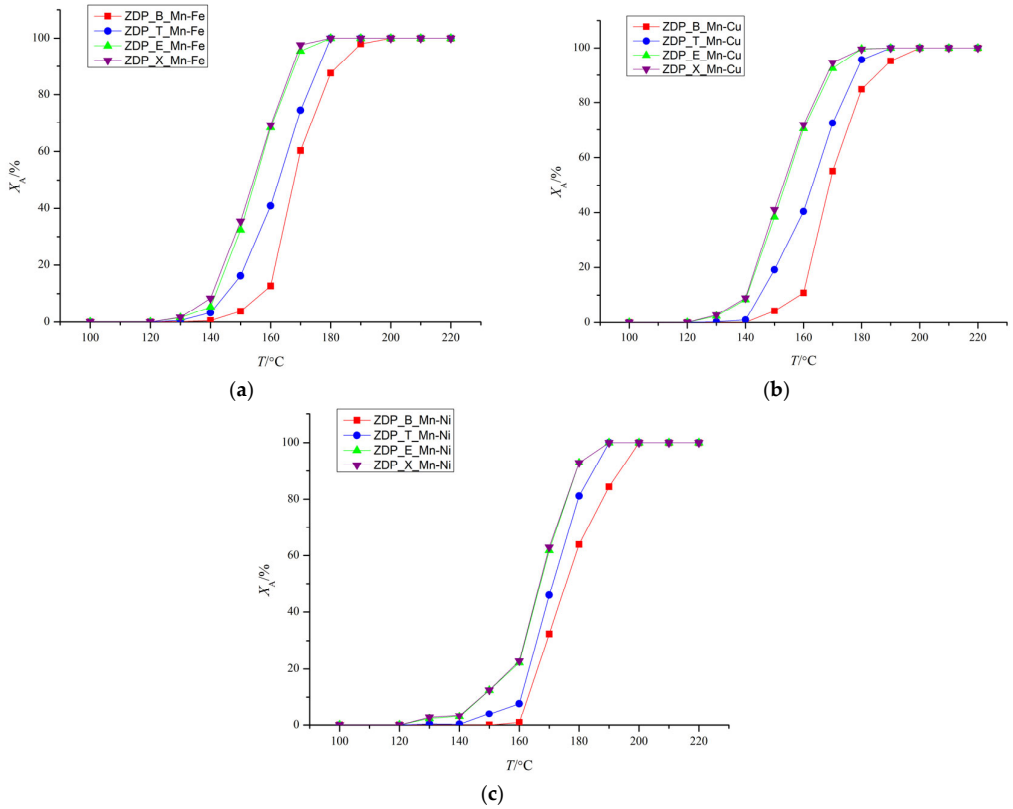

Figure 3. Comparison of the BTEX conversions at a reaction mixture flow rate of 92 cm^3/min using ZDP carriers with $MnFeO_x$ (**a**), $MnCuO_x$ (**b**), and $MnNiO_x$ (**c**) as catalytically active layers (B—benzene; T—toluene, E—ethylbenzene, and *o*-X—*o*-xylene).

Table 8. T_{10}, T_{50}, and T_{90} values (°C) for individual BTEX compounds using a ZDP catalyst carrier with $MnFeO_x$, $MnCuO_x$, and $MnNiO_x$ as the catalytically active layer.

Monolithic Carrier and Catalytic Layer	Benzene			Toluene			Ethylbenzene			*o*-Xylene		
	T_{10}	T_{50}	T_{90}	T_{10}	T_{50}	T_{90}	T_{10}	T_{50}	T_{90}	T_{10}	T_{50}	T_{90}
ZDP & $MnFeO_x$	157	168	183	146	163	176	142	155	168	143	155	168
ZDP & $MnCuO_x$	159	169	185	145	163	178	141	154	169	141	151	168
ZDP & $MnNiO_x$	163	176	194	161	172	185	148	167	179	148	167	179

It can be concluded that a 90% conversion of *o*-xylene and ethylbenzene is achieved at slightly lower temperatures than in the oxidation of toluene and benzene (Table 8). Considering the characteristic values of T_{10}, T_{50}, and T_{90}, the following order of reactivity can be determined during oxidation: *o*-xylene ≈ ethylbenzene < toluene < benzene. Since a 10%, 50%, and 90% conversion of benzene is achieved at higher temperatures compared to the other components, benzene was chosen as the criterion for the success of the oxidation. Therefore, it can be concluded that the catalyst with $MnFeO_x$ as the catalytic layer is the most effective, since the values mentioned were achieved at significantly lower temperatures compared to the other catalysts. The 90% benzene conversion is achieved for the catalyst mentioned at 183 °C, for the catalyst with $MnCuO_x$ catalytic layer it is achieved at 185 °C

and for the catalyst with $MnNiO_x$ at 194 °C, although the mass of the $MnNiO_x$ was the largest (39.5 mg).

The explanation for the better catalytic activity of $MnFeO_x$ compared to other manganese-based metal oxides, $MnMO_x$ (M: Fe, Ni, and Cu) has been given earlier [34]. Based on the results of XRD and XPS analyses, which confirmed the presence of the characteristic MnO_2, Mn_2O_3, and Fe_2O_3 phases, it seems that the Mn^{4+}, Mn^{3+}, and Fe^{3+} sites are responsible for the high activity of the $MnFeO_x$ catalyst, although it is not easy to distinguish their contribution. An overview of the mentioned crystal phases of powder $MnMO_x$ determined by our research group using XPS [34], XRD [34,35], and Raman spectroscopy [35] is given in Table S2. In addition, the high activity of $MnFeO_x$ catalysts for the oxidation of VOCs can probably also be attributed to the interaction between Mn and Fe species in the mixed oxide catalysts, which leads to the formation of defective manganese species and improves the catalyst activity. However, further experiments are still required to confirm this conclusion.

To gain a better insight into the behavior of the tested catalytic system, additional measurements were performed to investigate the contribution of homogeneous (thermal) oxidation of BTEX compounds. The tests were performed under identical conditions as the catalytic measurements but without the presence of a catalytic component, i.e., using a 3D-printed monolithic M support without a catalytic layer. The measurement results are shown in Figure S9, and the corresponding T_{10}, T_{50}, and T_{90} values are listed in Table S3. Our research group previously published results of similar measurements [36], without the use of catalyst support using the same reaction conditions, and reactor set-up. As can be seen in Figure S9, a slow trend of increasing conversion of all BTEX compounds was observed only at temperatures T > 250 °C, especially of benzene as the chemically most stable BTEX component. At the maximum operating temperature of 450 °C (due to safety reasons), no maximum conversion was achieved for any BTEX compound. The lowest conversions were obtained for benzene, and the maximum conversion of benzene was less than 20%. The conversions of toluene, ethylbenzene, and *o*-xylene were significantly higher and depended on the operating temperature. A comparison of the results in Table S3 with those shown in Table 8 indicates that the homogeneous (non-catalytic) oxidation of BTEX occurs at significantly higher temperatures, i.e., that the presence of the monolithic catalyst significantly increases the cost efficiency of the process, as it shifts the operating range for BTEX oxidation towards significantly lower temperatures.

Since $MnFeO_x$ proved to be the most effective catalytic layer in the previous step, the aforementioned catalytic layer was also applied to the other 3D-printed carriers (carriers with Z and M geometry). Table 9 shows the dimensions and geometric surfaces of the monolithic catalyst carriers used, as well as the mass of the catalytic layer applied. The geometric area of the carriers with Z and ZDP geometry was estimated from the CAD model, while the geometric area of the carrier with M geometry was determined experimentally by microscopy of the internal structure of the supports.

Table 9. Dimensions and geometric surfaces of the monolithic catalyst carriers used and the mass of the applied catalytic layer.

Geometry of the Monolithic Carrier	Dimensions/mm	Geometric Surface/cm^2	Mass of the Applied Catalytic Layer/mg
ZDP	6.11 ± 0.25 × 38.15 ± 0.06	30.1	33.7
Z	6.88 ± 0.32 × 38.13 ± 0.02	15.4	14.4
M	6.30 ± 0.26 × 36.77 ± 1.44	53.4	50.3

The catalytic activity test of the monolithic catalysts was carried out in the same way as described earlier, and the measurement results are shown in Figure 4. By determining the catalytic activity of 3D-printed carriers of different geometries, it was shown that the highest conversions, i.e., the lowest values of T_{10}, T_{50}, and T_{90}, are achieved with supports of geometry M. The temperature at which 90% conversion of benzene is achieved was 177 °C, 183 °C, and 197 °C for M-, ZDP- and Z-carrier, respectively. The results obtained were in line with expectations since the M-shaped catalyst carrier has the most complex geometry, the largest mass of the catalytic layer, and the largest surface area of the catalyst. The values of the T_{10}, T_{50}, and T_{90} listed in Table 10.

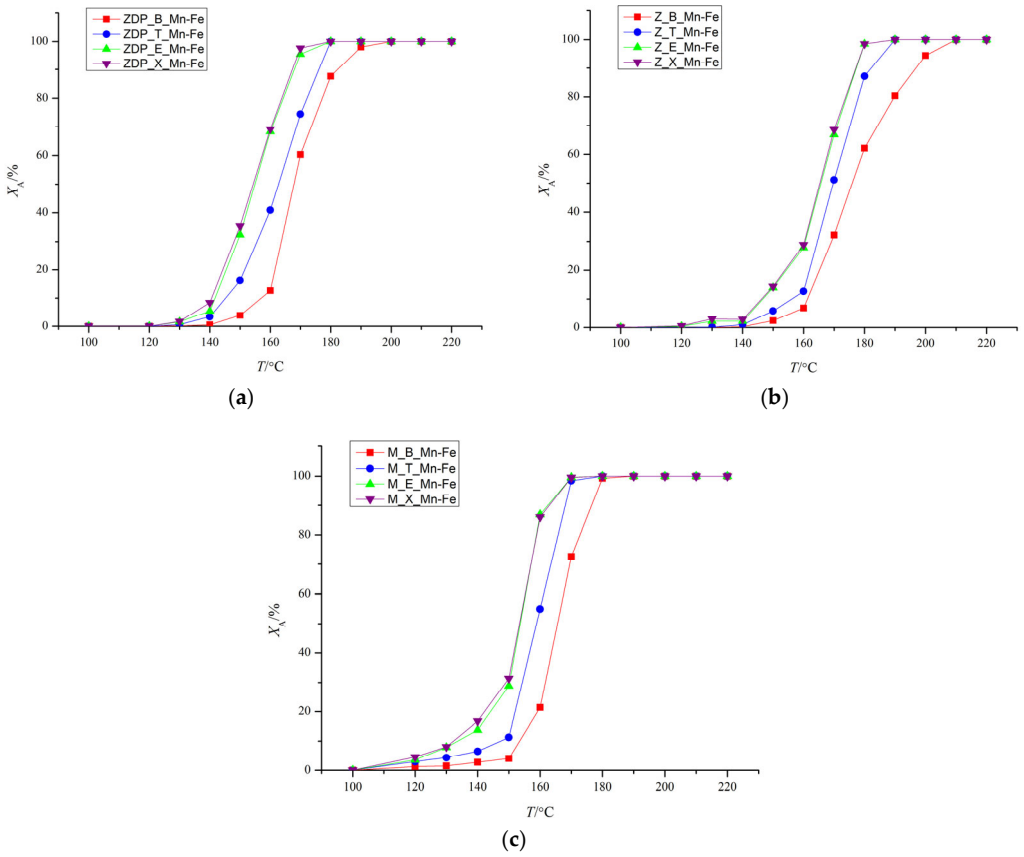

Figure 4. Comparison of BTEX conversions using ZDP (**a**), Z (**b**), and M (**c**) catalyst carriers for $MnFeO_x$ as the catalytically active layer (B—benzene, T—toluene, E—ethylbenzene, and X—*o*-xylene).

Table 10. T_{10}, T_{50}, and T_{90} values for individual BTEX compounds using ZDP catalyst carrier with $MnFeO_x$ as the catalytically active layer.

Monolithic Carrier and Catalytic Layer	Benzene			Toluene			Ethylbenzene			*o*-xylene		
	T_{10}	T_{50}	T_{90}	T_{10}	T_{50}	T_{90}	T_{10}	T_{50}	T_{90}	T_{10}	T_{50}	T_{90}
ZDP & $MnFeO_x$	157	168	183	146	163	176	142	155	168	143	155	168
Z & $MnFeO_x$	162	176	197	156	170	183	147	166	178	147	166	178
M & $MnFeO_x$	154	166	177	148	159	168	134	154	163	133	154	163

The most active monolith catalyst containing M catalyst carrier with $MnFeO_x$ as the catalytically active layer was tested in the oxidation of toluene after several cycles (Figure S10). Stability test was done at constant temperature of 170 °C at the constant total flow rate of 92 cm^3/min (80 cm^3/min of toluene and 12 cm^3/min of synthetic air) and at a constant inlet toluene concentration (51.3 ppm). The mass of the applied catalytic layer was 50 +/−

0.5 mg. The measurement results are displayed in Figure S10, and the corresponding T_{10}, T_{50}, and T_{90} values are listed in Table S2. It can be seen that the 3D-printed model M with $MnFeO_x$ exhibited very stable activity and stability even after several cycles under identical reaction conditions used, which is especially important for its application in real systems.

Finally, it should be emphasized that the appropriate geometry of the monolithic catalysts that can be fabricated using the advanced FFF technique, which includes the specific shape and number of channels, channel diameters, wall thickness, internal structure, etc., determines the overall geometric surface area on which the catalyst layer can be deposited. At the same time, a large open front surface and good accessibility of the active sites for the reactants should be ensured with the lowest possible pressure drop across such a structure. The advantages of such a specific geometry are only possible with monolithic and other similar types of structured catalysts/reactors and cannot be achieved with conventional catalyst configurations.

3. Materials and Methods

3.1. Materials

Monolithic catalyst carriers were prepared using fused filament fabrication (FFF, Flower Mound, TX, USA) technology from composite filament (1.75 mm in diameter) material based on zirconium dioxide (Zetamix, Keningau, Malaysia) as a ceramic component and polymer matrix, using 3D printer M200 (Zortrax, Olsztyn, Poland). On the obtained carriers, catalytic precursors were added using the following chemicals: $Mn(NO_3)_2 \times 4H_2O$ (Acros Organics, Geel, Belgium), $Cu(NO_3)_2 \times 3H_2O$ (Honeywell, Singapore), $Fe(NO_3)_3 \times 9H_2O$ (Fisher Chemical, Pittsburgh, PA, USA), and $Ni(NO_3)_2 \times 6H_2O$ (CARLO ERBA Reagents, Cornaredo, Italy). A gaseous BTEX mixture (Messer, Singapore) containing benzene (53.6 ppm), toluene (51.3 ppm), ethylbenzene (53.3 ppm), and *o*-xylene (50.7 ppm) in nitrogen was used to test the catalytic activity of the prepared catalysts in the temperature range between room temperature and 220 °C under atmospheric pressure.

3.2. Preparation of Ceramic Monolithic Catalyst Carriers

The 3D-CAD models of the desired monolithic catalyst carriers were created using the software Autodesk Fusion 360, and prior to 3D printing, they were loaded into the so-called "slicer" Z-SUITE for the purpose of preparing the model for 3D printing. In the Z-SUITE, 3D printing settings were set, which included defining the support structure, selecting the shape and density of the internal structures, changing dimensions along the x-, y-, and z-axes; print speed; layer thickness (resolution); extruder flow ratio; and fan speed (significant impact on cooling rate). Once the printing process is complete, the support structure must be detached from the substrate using two-stage debinding (chemical and thermal), as described in the filament user manual [37]. The support structure is carefully removed in two steps. During chemical debinding, the 3D-printed carrier was immersed in an acetone solution for 2 h and then dried at 100 °C until the acetone was completely removed. In the next step, the dried monoliths were heated up to 500 °C using 8 °C/h ramp in a high-temperature oven.

After debinding, monoliths need to be sintered by gradually increasing the temperature from 20 °C to 1475 °C at a heating rate of 50 °C/h. The temperature is then kept constant at 1475 °C for 2 h to ensure representative sintering of the ceramic particles. The temperature is then gradually reduced to room temperature (15–18 h) to prevent temperature shocks of the obtained monolithic catalyst carriers.

The filament (wire) used in this study was a commercial product manufactured by Zetamix, prepared through a standard hot extrusion process at their facility. As the focus of research was on the subsequent processing and application, the filament was utilized

as provided by the manufacturer without modifications. The mixture used for extrusion and printing contains ceramic particles, which can have abrasive properties. To address this, a hardened steel nozzle was used which is better suited to handle abrasive materials compared to standard brass nozzles. The nozzle was monitored regularly during the printing process and showed no significant wear, so it was not necessary to change the nozzle throughout the experiments.

3.3. Optimal Printing Settings

The optimal print settings had to be defined before the beginning of the 3D printing of monolithic catalyst carriers that will be used in the reactor. For this purpose, various settings such as extruder flow ratio, layer thickness, printing speed, and fan speed were tested on a simple tile models (20 mm × 10 mm × 2 mm) In addition, five printed plates (using optimal 3D printing settings) were printed to evaluate the mechanical stability of the catalytic layer (adhesion test).

3.4. Preparation of Washcoated Monolithic Catalysts

Catalytically active components were applied to the 3D-printed monolithic carriers using the wet impregnation technique. The printed monolithic carriers need to be pre-washed in a 96% ethanol to remove possible impurities. After the washing process, the monolithic carriers were dried at 100 °C, followed by application of the catalytic precursors using wet impregnation. For this purpose, 1 mol/dm^3 catalytic precursor solutions were prepared by dissolving $Mn(NO_3)_2 \times 4H_2O$, $Cu(NO_3)_2 \times 3H_2O$, $Fe(NO_3)_3 \times 9H_2O$ and $Ni(NO_3)_2 \times 6H_2O$ in deionized water.

To find the best catalyst for the removal of BTEX compounds, three different catalytic precursor solutions were prepared. The impregnation solutions were prepared by mixing 10 mL of $Mn(NO_3)_2 \times 4H_2O$ solution with 10 mL of $Fe(NO_3)_3 \times 9H_2O$ solution, $Cu(NO_3)_2 \times 3H_2O$, or $Ni(NO_3)_2 \times 6H_2O$ solution. An individual monolithic catalyst carrier was fully submerged in the prepared solutions for 15 min and occasionally stirred/shaken in order to remove air bubbles from the carrier.

The monoliths are subsequently dried at 100 °C for 1 h to remove remaining water after impregnation. This step is crucial because the sudden, high-temperature evaporation of water during calcination could cause cracking of the monolith. After drying, the monoliths were calcined at 500 °C for 2 h (using temperature ramp of 2.5 °C/min). During calcination, catalytic precursors (nitrate salts) oxidize and form catalytically active mixed manganese oxides.

3.5. Characterization Methods

3.5.1. X-Ray Diffraction Analysis (XRD)

The crystalline phase of the sample was identified using an X-ray diffractometer XRD 6000 (Shimadzu, Tokyo, Japan) with CuKα radiation (λ = 1.5406 Å). A voltage of 40 kV was used, with a current of 30 mA. The analysis was performed in the 2θ range between 5° and 85° with a step size of 0.02° and a measurement time of 0.6 s per step.

3.5.2. Size Distribution of Ceramic Particles

The ceramic particle size distribution was determined by laser diffraction analysis (LDA). The laser diffractometer SALD-3101 (Shimadzu) was used for this analysis. From the obtained results, the characteristic diameters were determined: d_{50} as a median diameter, d_{mode} as a dominant size of particles in the population, and $d_{3,2}$ as a Sauter mean diameter using the differential distribution function, $dQ_3(d)$.

3.5.3. TGA/DTA Analysis

In this work, a simultaneous thermogravimetric (TGA) and differential thermal analysis (DTA) was carried out using the STA 409 simultaneous thermal analyzer (Netzsch, Exton, PA, USA). The analysis was carried out in the temperature range from room temperature to 1400 °C, with a sample heating rate of 10 °C/min. The test was carried out in an inert nitrogen atmosphere, with the introduction of air at 600 °C.

3.5.4. Deviations in Dimensions and Mass of the 3D-Printed Catalyst Carriers

As a result of heat treatment of 3D-printed models, their shrinkage occurs along all three coordinate axes. For this reason, it is crucial to determine the correction factor by which the CAD model needs to be enlarged before printing. The test was carried out by measuring the 3D-printed models at five different points along the x-, y-, and *z*-axes with a digital caliper (Alpha Tools). Based on the collected data, the mean value for each axis was calculated, and the standard deviation was defined.

The mass deviation was determined by weighing the 3D-printed models of the same geometry before and after thermal treatment. The mass was measured using an analytical laboratory balance, AS 220.R2 (RADWAG; Radom, Poland). This test gives an insight not only into the proportion of the ceramic phase in the material based on the mass loss that occurs due to the decomposition of the polymer phase of the material but also into the uniformity of the distribution of ceramic particles in the carrier.

3.5.5. Adhesion Test

An adhesion test was carried out to determine the mechanical stability of the catalytic layer. Five 20 mm × 10 mm × 2 mm 3D-printed plates were used (as a preliminary test), to which the catalyst was applied using the same methodology as described in Section 3.4. The test was also performed using the ZDP, Z, and M catalyst carriers (Figures 1 and 2). The tested specimen was immersed in petroleum ether and subjected to ultrasonic vibrations in an Elmasonic S 30 H (Elma, Fremont, CA, USA) ultrasonic bath with an operating frequency of 37 kHz for 30 min at room temperature. Petroleum ether was used, as it does not react chemically with the 3D-printed carriers, nor with the applied catalysts; therefore, it can be safely asserted that potential losses of the catalyst as a result of the conducted test are the result of the poor adhesion of the catalyst to the carrier. The catalysts are then dried at 100 °C and weighed. The mass of the catalyst is compared both before and after the adhesion test to evaluate the mechanical stability of the catalyst.

3.6. Catalytic Oxidaton of BTEX Compounds

BTEX compounds were catalytically oxidized in a monolithic reactor at atmospheric pressure, different temperatures, and a constant total flow rate of 92 cm^3/min (80 cm^3/min of BTEX and 12 cm^3/min of synthetic air) for the reaction mixture, as well as a constant volume ratio of the BTEX and synthetic air (oxidant) mixture.

The apparatus consists of a monolithic reactor, temperature control unit (TCU), two mass flow controllers (MFCs) for the flow of synthetic air and BTEX mixture, a computer for data acquisition and processing, and a gas chromatograph (GC-2014, Shimadzu) equipped with a flame ionization detector (FID) for analysis of the reaction mixture at the outlet of the reactor. The catalytic activity of previously prepared monolithic catalysts with varying geometries and catalytically active components was evaluated during the experiments. The temperature in the reactor was monitored using a thermocouple positioned inside the reactor, above the monolithic catalyst.

4. Conclusions

The aim of this work was to develop 3D-printed ceramic monolithic catalysts and to test their catalytic activity for the oxidation of the gaseous BTEX mixture. It was found that ceramic monolithic catalyst carriers of the defined geometry can be successfully produced using the fused filament fabrication (FFF) technique. Using the wet impregnation technique, catalytic layers consisting of mixed oxides of Mn, Fe, Cu, and Ni were successfully deposited on 3D-printed catalyst carriers. XRD analysis of the ZrO_2 filament revealed that the ceramic phase of the material consists of monoclinic and tetragonal ZrO_2. A dimensional correction factor of 1.20 was determined by testing the deviation of the 3D-printed carriers' dimensions after the heat treatment in comparison with the theoretical CAD models. Based on the mass deviation tests of the 3D-printed catalyst carriers, a uniform distribution of the ceramic particles was determined. Adhesion tests showed insignificant loss of the catalyst (<1%) due to the influence of ultrasonic vibrations. This confirmed the exceptional stability of the catalytic layer, which is of great importance for the application of the monolithic catalyst in a reactor. It was experimentally confirmed that the most efficient catalyst contains the mixed oxide $MnFeO_x$ as the catalytically active component. When comparing the catalytic activity of 3D-printed ceramic catalyst carriers with different geometries (ZDP, Z, and M), the 3D-printed model M proved to be the most successful design for the oxidation of a mixture of BTEX compounds, due to the highest surface area and catalyst load.

Supplementary Materials: The following supporting information can be downloaded at https://www.mdpi.com/article/10.3390/catal15020125/s1: Figure S1: CAD model of 3D-printed catalyst carrier M; Figure S2: Three-dimensional-printed model with default 3D printing settings; Figure S3: Three-dimensional-printed model with EFR print settings (from left to right): −20%, −40%, and −50%; Figure S4: Monolithic catalyst carrier with ZDP geometry, obtained by optimizing the settings and increasing the cooling rate of the material; Figure S5: Catalyst carriers ZDP (left) and Z (right) 3D-printed using optimal 3D printing settings; Figure S6: X-ray diffractogram of theZrO2-based composite filament; Figure S7: Size distribution of ceramic particles in ZrO2-based filament; Figure S8: Results of simultaneous TGA/DTA analysis of the ZrO2-based filament; Figure S9: Homogeneous oxidation of BTEX on a monolithic support without a catalytic layer at a total reaction mixture flow rate of 92 mL/min (B—benzene; T—toluene, E—ethylbenzene, and X—o-xylene); Figure S10: Repeated catalytic tests of toluene oxidation. The catalytic evaluation was performed 3 times under the same reaction conditions. Stability performance using M catalyst carrier with MnFeOx at constant inlet flow rate of the toluene (92 cm3/min) and constant inlet toluene concentration (51.3 ppm); Table S1: Weight hourly space velocity (WHSV) values using Z, ZDP, and M catalyst carriers during homogenous oxidation of BTEX compounds; Table S2: Insight into the crystalline phases of powder MnMOx (M: Fe, Cu, and Ni) catalyst determined by XPS, XRD, and Raman spectroscopy; Table S3: T10, T50, and T90 values for individual BTEX compounds using ZDP monolith without catalytic layer at a reaction mixture flow rate of 92 mL/min during homogenous oxidation of BTEX compounds.

Author Contributions: Conceptualization, F.C., D.V. and V.T.; methodology, F.C. and D.V.; validation, F.C. and V.T.; formal analysis, F.C. and N.Z.; investigation, F.C. and N.Z.; resources, V.T. and D.V.; data curation, F.C. and N.Z.; writing—original draft preparation, F.C., N.Z. and V.T.; writing—review and editing, F.C., V.T. and D.V.; visualization, F.C. and D.V.; supervision, V.T.; project administration, F.C. and D.V.; funding acquisition, V.T. and D.V. All authors have read and agreed to the published version of the manuscript.

Funding: This work was supported by the Croatian Science Foundation under the projects IN-PhotoCat (IP-2018-01-8669) and INDIGO (IP-2022-10-8004).

Data Availability Statement: The original contributions presented in the study are included in the article, further inquiries can be directed to the corresponding author.

Conflicts of Interest: The authors declare no conflicts of interest.

References

1. Guan, Z.; Yang, X.; Liu, P.; Xu, X.; Li, Y.; Yang, X. Additive manufacturing of zirconia ceramic by fused filament fabrication. *Ceram. Int.* **2023**, *49*, 27742–27749. [CrossRef]
2. Brischetto, S.; Maggiore, P.; Ferro, C. Special Issue on "Additive Manufacturing Technologies and Applications". *Technologies* **2017**, *5*, 58. [CrossRef]
3. Cai, X.; Yang, M.; Qiao, Y.; Wang, Z.; Zhou, J.; Xue, F. Experimental investigation on wear resistance and corrosion behavior of nickel-aluminum bronze alloy fabricated by wire-arc additive manufacturing. *J. Mater. Res. Technol.* **2023**, *26*, 5801–5815. [CrossRef]
4. Spiller, S.; Olsøybakk Kolstad, S.; Razavi, N. Fatigue behavior of 316L stainless steel fabricated via Material Extrusion Additive Manufacturing. *Eng. Fract. Mech.* **2023**, *291*, 109544. [CrossRef]
5. Staudacher, M.; Lube, T.; Glettler, J.; Scheithauer, U.; Schwentenwein, M. A novel test specimen for strength testing of ceramics for additive manufacturing. *Open Ceram.* **2023**, *15*, 100410. [CrossRef]
6. Bánhegyi, G. Polymer compatibility and interfaces in extrusion-based multicomponent additive manufacturing—A mini-review. *Adv. Ind. Eng. Polym. Res.* **2023**, *7*, 428–453. [CrossRef]
7. Guo, N.; Leu, M.C. Additive manufacturing: Technology, applications and research needs. *Front. Mech. Eng.* **2013**, *8*, 215–243. [CrossRef]
8. Zhu, J.; Wu, P.; Chao, Y.; Yu, J.; Zhu, W.; Liu, Z.; Xu, C. Recent advances in 3D-printing for catalytic applications. *Chem. Eng. J.* **2022**, *433*, 134341. [CrossRef]
9. Großmann, P.F.; Tonigold, M.; Szesni, N.; Fischer, R.W.; Seidel, A.; Achterhold, K.; Pfeiffer, F.; Rieger, B. Influence of internal and external surface area on impregnation and activity of 3D-printed catalyst carriers. *Catal. Commun.* **2023**, *175*, 106610. [CrossRef]
10. Madhavadas, V.; Srivastava, D.; Chadha, U.; Aravind Raj, S.; Sultan, M.T.H.; Shahar, F.S.; Shah, A.U.M. A review on metal additive manufacturing for intricately shaped aerospace components. *CIRP J. Manuf. Sci. Technol.* **2022**, *39*, 18–36. [CrossRef]
11. Zhao, N.; Parthasarathy, M.; Patil, S.; Coates, D.; Myers, K.; Zhu, H.; Li, W. Direct additive manufacturing of metal parts for automotive applications. *J. Manuf. Syst.* **2023**, *68*, 368–375. [CrossRef]
12. Chang, S.-Y.; Jin, J.; Yan, J.; Dong, X.; Chaudhuri, B.; Nagapudi, K.; Ma, A.W.K. Development of a pilot-scale HuskyJet binder jet 3D-printer for additive manufacturing of pharmaceutical tablets. *Int. J. Pharm.* **2021**, *605*, 120791. [CrossRef]
13. Rouf, S.; Malik, A.; Singh, N.; Raina, A.; Naveed, N.; Siddiqui, M.I.H.; Haq, M.I.U. Additive manufacturing technologies: Industrial and medical applications. *Sustain. Oper. Comput.* **2022**, *3*, 258–274. [CrossRef]
14. Saleh Alghamdi, S.; John, S.; Roy Choudhury, N.; Dutta, N.K. Additive Manufacturing of Polymer Materials: Progress, Promise and Challenges. *Polymers* **2021**, *13*, 753. [CrossRef] [PubMed]
15. Govender, S.; Friedrich, H. Monoliths: A Review of the Basics, Preparation Methods and Their Relevance to Oxidation. *Catalysts* **2017**, *7*, 62. [CrossRef]
16. Nijhuis, T.A.; Beers, A.E.W.; Vergunst, T.; Hoek, I.; Kapteijn, F.; Moulijn, J.A. Preparation of monolithic catalysts. *Catal. Rev.* **2001**, *43*, 345–380. [CrossRef]
17. Tsai, S.-B.; Ma, H. A Research on Preparation and Application of the Monolithic Catalyst with Interconnecting Pore Structure. *Sci. Rep.* **2018**, *8*, 16605. [CrossRef]
18. Deraz, N.M. The comparative jurisprudence of catalysts preparation methods: I. precipitation and impregnation methods. *J. Ind. Environ. Chem.* **2018**, *2*, 19–21.
19. Yao, D.; Yang, H.; Chen, H.; Williams, P.T. Co-precipitation, impregnation and so-gel preparation of Ni catalysts for pyrolysis-catalytic steam reforming of waste plastics. *Appl. Catal. B Environ.* **2018**, *239*, 565–577. [CrossRef]
20. Li, K.; Luo, X. Research Progress on Catalytic Combustion of Volatile Organic Compounds in Industrial Waste Gas. *Catalysts* **2023**, *13*, 268. [CrossRef]
21. Chen, X.; Li, J.; Wang, Y.; Zhou, Y.; Zhu, Q.; Lu, H. Preparation of nickel-foam-supported Pd/NiO monolithic catalyst and construction of novel electric heating reactor for catalytic combustion of VOCs. *Appl. Catal. A Gen.* **2020**, *607*, 117839. [CrossRef]
22. Hao, R.; Sun, J.; Liu, R.; Zhao, H.; Yao, Z.; Wang, H.; Hao, Z. Emission characteristics, environmental impact, and health risk assessment of volatile organic compounds (VOCs) during manicure processes. *Sci. Total Environ.* **2024**, *906*, 167464. [CrossRef] [PubMed]
23. Pandey, P.; Yadav, R. A Review on Volatile Organic Compounds (VOCs) as Environmental Pollutants: Fate and Distribution. *Int. J. Environ.* **2018**, *4*, 14–26. [CrossRef]
24. Air Quality Guidelines for Europe. Available online: https://www.who.int/publications/i/item/9789289013581 (accessed on 21 November 2023).
25. Lou, B.; Shakoor, N.; Adeel, M.; Zhang, P.; Huang, L.; Zhao, Y.; Zhao, W.; Jiang, Y.; Rui, Y. Catalytic oxidation of volatile organic compounds by non-noble metal catalyst: Current advancement and future prospectives. *J. Clean. Prod.* **2022**, *363*, 132523. [CrossRef]

26. Hao, Z.; Ma, Y.; Chen, Y.; Fu, P.; Wang, P. Non-Noble Metal Catalysts in Cathodic Oxygen Reduction Reaction of Proton Exchange Membrane Fuel Cells: Recent Advances. *Nanomaterials* **2022**, *12*, 3331. [CrossRef]
27. Kim, H.-S.; Kim, H.-J.; Kim, J.-H.; Kim, J.-H.; Kang, S.-H.; Ryu, J.-H.; Park, N.-K.; Yun, D.-S.; Bae, J.-W. Noble-Metal-Based Catalytic Oxidation Technology Trends for Volatile Organic Compound (VOC) Removal. *Catalysts* **2022**, *12*, 63. [CrossRef]
28. Xu, H.; Yan, N.; Qu, Z.; Liu, W.; Mei, J.; Huang, W.; Zhao, S. Gaseous Heterogeneous Catalytic Reactions over Mn-Based Oxides for Environmental Applications: A Critical Review. *Environ. Sci. Tech.* **2017**, *51*, 8879–8892. [CrossRef]
29. Kim, S.C.; Shim, W.G. Catalytic combustion of VOCs over a series of manganese oxide catalysts. *Appl. Catal. B Environ.* **2010**, *98*, 180–185. [CrossRef]
30. Mangla, O.; Roy, S. Monoclinic Zirconium Oxide Nanostructures Having Tunable Band Gap Synthesized under Extremely Non-Equilibrium Plasma Conditions. *Proceedings* **2019**, *3*, 10. [CrossRef]
31. Lin, Y.F.; Liang, F.L. Synthesis of a ZrO_2/carbon aerogel composite with tetragonal ZrO_2 structures assisted by the formation of phenol formaldehyde resin. *Cryst. Eng. Comm.* **2015**, *17*, 678–685. [CrossRef]
32. Aguilar, D.H.; Torres-Gonzalez, L.C.; Torres-Martinez, L.M.; Lopez, T.; Quintana, P. A Study of the Crystallization of ZrO_2 in the Sol–Gel System: ZrO_2–SiO_2. *J. Solid State Chem.* **2001**, *158*, 349–357. [CrossRef]
33. Rani, S.; Verma, S.; Kumar, S. Tailoring the structural and optical parameters of zirconia nanoparticles via silver. *Appl. Phys. A* **2017**, *123*, 539. [CrossRef]
34. Duplančić, M.; Gomzi, V.; Pintar, A.; Kurajica, S.; Tomašić, V. Experimental and theoretical (ReaxFF) study of manganese-based catalysts for low-temperature toluene oxidation. *Ceram. Int.* **2021**, *47*, 3108–3121. [CrossRef]
35. Car, F.; Gomzi, V.; Tomašić, V.; Vrsaljko, D.; Kurajica, S. Development of Novel Monolithic Catalyst for BTEX Catalytic Oxidation Using 3D Printing Technology. *ChemEng* **2025**, *9*, 9. [CrossRef]
36. Car, F.; Sušec, I.; Tomašić, V. Preparation and Testing of Cordierite Monolithic Catalysts for Oxidation of Aromatic Volatile Organic Compounds. *Chem. Eng. Trans.* **2021**, *86*, 673–678. [CrossRef]
37. Zetamix General Guidelines White Zirconia. Available online: https://zetamix.fr/wp-content/uploads/2022/10/Guideline-White-Zirconia.pdf (accessed on 23 November 2023).